


# Maxillary Sinus Lift with Beta-Tricalcium Phosphate ( $\beta$ -TCP) in Edentulous Patients: A Nanotomographic and Raman Study

Florence Pascaretti-Grizon<sup>1</sup> · Bernard Guillaume<sup>1,2</sup> · Lisa Terranova<sup>1</sup> · Baptiste Arbez<sup>1</sup> · H el ene Libouban<sup>1</sup> · Daniel Chappard<sup>1,3</sup> 

Received: 13 December 2016 / Accepted: 10 April 2017  
  Springer Science+Business Media New York 2017

**Abstract** Sinus lift elevation restores bone mass at the maxilla in edentulous patients before the placement of dental implants. It consists of opening the lateral side of the sinus and grafting beta-tricalcium phosphate granules ( $\beta$ -TCP) under the olfactory membrane. Bone biopsies were obtained in five patients after 60 weeks. They were embedded undecalcified in poly(methyl methacrylate) (pMMA); blocks were analyzed by nanocomputed tomography (nanoCT); specific areas were studied by Raman microspectroscopy. Remnants of  $\beta$ -TCP were osseointegrated and covered with mineralized bone; osteoid tissue was also filling the inner porosity. Macrophages having engulfed numerous  $\beta$ -TCP grains were observed in marrow spaces.  $\beta$ -TCP was identified by nanoCT as osseointegrated particles and as granules in the cytoplasm of macrophages. Raman microspectroscopy permitted to compare the spectra of  $\beta$ -TCP and bone in different areas. The ratio of the  $\sim 820\text{ cm}^{-1}$  band of pMMA ( $-\text{CH}_2$  groups) on the  $\nu_1$  phosphate band at  $960\text{ cm}^{-1}$  reflected tissue hydration because water was

substituted by MMA during histological processing. In bone, the ratio of the  $\sim 960\text{ cm}^{-1}$  phosphate to the amide I band and the ratio  $\nu_2$  phosphate band by the 1240–1250 amide III band reflect the mineralization degree. Specific bands of  $\beta$ -TCP were found in osseointegrated  $\beta$ -TCP granules and in the grains phagocytized by the macrophages. The hydration degree was maximal for  $\beta$ -TCP phagocytized by macrophages. Raman microspectroscopy associated with nanoCT is a powerful tool in the analysis of the biomaterial degradation and osseointegration.

**Keywords**  $\beta$ -TCP · Raman microspectroscopy · Nanotomography · Sinus lift · Bone graft · Tricalcium phosphate

## Introduction

Several types of biomaterials are available for filling bone defects or performing bone graft to restore a suitable bone volume and microarchitecture. Granules of biomaterials are often used because they can easily fill a bone cavity (e.g., alveolar pouch after a tooth extraction, a bone cyst or a larger defect, sinus lifting before dental implant placement) [1, 2]. Various types of biomaterials can be prepared in the granular form including morcellized autograft, cleaned and purified allo- or xenogeneic bone, natural biomaterials (coral or mother of pearl particles), and pure synthetic calcium phosphate biomaterials ( $\beta$ -tricalcium phosphate ( $\beta$ -TCP), hydroxyapatite). The interest of using granules is to obtain a complete filling of the cavity, a condition that cannot be achieved using compact blocks of materials. It has been found that granules, gently packed in the grafted area, maintain a 3D macroporosity which depends on the size and microarchitecture of the granules themselves

**Electronic supplementary material** The online version of this article (doi:10.1007/s00223-017-0280-5) contains supplementary material, which is available to authorized users.

✉ Daniel Chappard  
daniel.chappard@univ-angers.fr

- <sup>1</sup> GEROM Groupe Etudes Remodelage Osseux et bioMat eriaux, NextBone, IRIS-IBS Institut de Biologie en Sant e, CHU d'Angers, Universit e d'Angers, 49933 Angers Cedex, France
- <sup>2</sup> CFI, Coll ege Fran ais d'Implantologie, 6, rue de Rome, 75005 Paris, France
- <sup>3</sup> GEROM – NextBone, IRIS-IBS Institut de Biologie en Sant e, CHU d'Angers, 49933 Angers Cedex, France

[3, 4].  $\beta$ -TCP granules can be prepared with different formulations and the macroporosity created between the granules represents the space available for vascular invasion and, subsequently, the migration of osteoprogenitor cells [4]. Animal and human studies have found that bone apposition is associated with resorption of the biomaterial. A stack of  $\beta$ -TCP granules represents a suitable scaffold serving for the anchorage of bone at the surface of the granules associated with a direct resorption by mononucleated macrophages and osteoclasts [5–8]. Macrophages belong to the immune system, and interaction between bone remodeling cells and the immune system has led to the development of the concept of ‘osteimmunology’ [9]. Macrophages directly interact with biomaterials whose chemical composition influences the nature of the macrophagic response: M1 macrophages induce an inflammatory and fibrotic response, while M2 macrophages are immunosuppressive and favor wound healing [10–12]. It has been found that macrophages play a key role in  $\beta$ -TCP-induced osteogenesis and favor osteoblastogenesis from stromal cells present in the bone marrow [13]. Degradation of  $\beta$ -TCP by macrophages implies adherence of the cell at the surface of the material and erosion by phagocytosis of minute grains that have been sintered during the preparation steps of the granules. Histological analyses performed on undecalcified sections have revealed numerous macrophages with a cytoplasm filled with  $\beta$ -TCP [5, 6, 14]. Several authors have reported that these cells express carbonic anhydrase, an enzyme necessary to proceed  $H^+$  ions used for decalcification [15, 16]. In addition, they can also express TRAcP (tartrate-resistant acid phosphatase), an enzyme necessary to complete the intracellular digestion of collagen in osteoclasts [5, 17–19].

The aim of the present study was to analyze, in a series of patients having had a sinus lift with  $\beta$ -TCP granules, the morphological characteristics of the biomaterial degradation and osseointegration using X-ray nanotomography. The degradation of the biomaterial was searched by Raman microspectroscopy on the different locations of  $\beta$ -TCP on the tissue blocks.

## Materials and Methods

### $\beta$ -TCP Granules

$\beta$ -TCP granules used in this study were produced by Kasios (L’Union—France) using the polyurethane foam technology [20, 21]. The product composition was verified using an X-ray diffractometer (XRD; Bruker D8 A25 Discover) using  $Cu K\alpha$  radiation operated at 40 kV and 40 mA in the  $2\theta$  range of  $25^\circ$ – $45^\circ$ . The resulting trace was analyzed and compared with the standard library of known diffraction

patterns (JCPDS). The surface morphology was observed by scanning electron microscopy (JEOL 6301F, Paris, France). The  $\beta$ -TCP granules were glued on an aluminum stub with a double-sided carbon sellotape. They were gold-coated by sputtering with a MED 020 (Bal-Tec, Chatillon sur Cher, France). Images were captured at a 3 kV acceleration voltage in the secondary electron mode. Some granules were then embedded in poly(methyl methacrylate) (pMMA) in the same conditions as bone biopsies (see further).

### Patients and Surgical Protocol

Five patients who presented a complete tooth loss at the maxilla and who were candidate for implant placing after a bone graft were enrolled in the study. Each gave her/his informed consent to participate in the present study. This experimental protocol was approved by the ethical committee of the French Collège d’Implantologie and was done in accordance with the institutional guidelines of the French Ethical Committee and with the 1964 Helsinki declaration and its later amendments. The surgical protocol aimed at increasing the thickness of the sinus floor using  $\beta$ -TCP granules. The thickness of the sinus floor was appreciated on CT scans before sinus lift elevation. A control CT scan was performed before the placement of dental implants of standard diameter. The bone graft was harvested at the chin and the chips of cortico-trabecular bone were obtained and mixed with the patient’s blood together with  $\beta$ -TCP granules to obtain a kind of paste containing 10% autograft that could be handled more easily.

The grafted area was prepared as follows: the mucoperiosteal flap was removed after a lateral osteotomy on the external face of the maxillary sinus (usually the opening is 15 mm in length and 10 mm in height). The Schneiderian membrane was gently pushed through the window, away from the bone to avoid perforation. The mixture containing autograft particles,  $\beta$ -TCP, and blood was inserted into the void space, under the membrane. Usually, a thickness of several millimeters of the ‘paste’ was added to reconstitute a suitable volume that will support the placement of implants after healing. The full thickness flap was then closed to the primary incisions and sutured with 4/0 Vicryl<sup>TM</sup> (Ethicon SAS, Issy Les Moulineaux, France).

### Bone Biopsy Harvesting

About thirty weeks after the bone graft, the implants were placed in the maxilla. A small bone core was removed with a dental trephine (Dexter, H. Zepf, Ref 08910 02/CE 01202/05, Argenteuil, France) with a 2.3 mm internal diameter and 2.8 mm external diameter, mounted on a contra-angle attachment. Bone biopsies were immediately

transferred into Beebe's fixative at 4 °C in a refrigerator (ethanol 75%, formalin 10%, distilled water 15%) during 24 h and dehydrated with absolute acetone [22]. Samples were received in the laboratory and embedded undecalcified in pMMA. During the histological processing of the biopsy, the tissues were dehydrated in acetone. Clearing in xylene substitutes acetone in a second step and finally, methyl methacrylate used during the infiltration step, replaces xylene. Only recently, it has been reported that the fraction of pMMA in a bone tissue represents the diffusion space corresponding to the initial fraction of water (i.e., the hydration of the tissue) [23]. Sections (7  $\mu$ m in thickness) were cut dry on a heavy duty microtome equipped with tungsten carbide knives (Leica Polycut S with 50° knives). They were stained with Goldner's trichrome for the identification of osteoid tissue (recently formed and uncalcified bone), and toluidine blue for cell analysis, as previously described [24].

### Nanocomputed Tomography (nanoCT)

Remnants of the blocks (half of the biopsy in thickness) were transferred in a X-ray computed nanotomograph (Nanotom, Phoenix, GE, USA). NanoCT analysis was done at 65 kV and 450  $\mu$ A using a copper filter. Five projection images were averaged every 750 ms and the rotation angle was 1.95°/min with a pixel size of 0.7  $\mu$ m. Image reconstruction was done on the projection images with the DATOS software (Phoenix, GE) and a stack of 2D sections was obtained for each specimen. 3D models were obtained with VG StudioMax (Volume Graphics GmbH, Heidelberg, Germany).

### Raman Microspectroscopy

The blocks were polished to a 1  $\mu$ m finish with diamond particles on a grinding machine (Struers, France) and analyzed on a Senterra Raman microscope with the OPUS 5.5 software (Bruker optic, Ettlingen, Germany). A laser beam was focused on the surface of the block to a micrometer spot size through an Olympus BX51 microscope with a 50 $\times$  objective. Because bone has a strong auto-fluorescence, the excitation laser wavelength was 785 nm with an excitation power of 100 mW and 8.12  $\text{cm}^{-1}$  resolution. To obtain a given spectrum, 5 scans of 15 s were averaged in each case. Spectra were obtained on the areas previously identified by nanoCT and imaged with the video epi-illumination of the Senterra microscope. An automatic baseline was applied on all spectra (fitting based on a  $x^{11}$  polynomial function). Raman analysis of the raw  $\beta$ -TCP material was also obtained in two different conditions: crude granules directly provided by the manufacturer in sterile vials and the same granules after

embedding in pMMA as above. In this last case, blocks were trimmed and polished to expose the granules at the surface of the block. The spectrum of pMMA used for embedding the biopsy was analyzed in search of typical representative bands that can be used to derive the degree of hydration (or microporosity) of the tissue or the bio-material considered [23]. The spectrum of the patients' bone was obtained at distance from the remaining granules, usually in the cortical bone. They were compared to the spectrum obtained on a piece of human bone unembedded, after pMMA embedding and after demineralization to analyze the collagen of the organic phase of the bone matrix. Other spectra of bone were observed in different locations within the biomaterial and inside the phagocytic cells. For each location, the spectra were obtained in at least 3 areas. For the determination of the ratios of band peaks, the values of all patients were averaged.

In the case of bone tissue, it is possible to determine the degree of mineralization (or mineral to organic matrix ratio) of the matrix as the ratio of the  $\nu_1$  phosphate band by the 1590–1720  $\text{cm}^{-1}$  amide I band, as previously reported [25]. Other authors have proposed the ratio of the  $\nu_2$  phosphate band by the 1240–1250 amide III band [26].

## Results

### $\beta$ -TCP Granules

The granules' composition consisted of phase pure and highly crystalline  $\beta$ -TCP as verified by XRD (Fig. 1). The resulting trace was analyzed and was found similar with the standard library of known diffraction patterns (JCPDS N° 9-69). The geometry of the polyurethane foam produced concave surfaces and macroporosity of the  $\beta$ -TCP granules (Fig. 2a). An inner porosity, left by the polyurethane foam, was also well defined in the form of triangular profiles connected with grooves. The free surface of the granules was formed by a pavement of polygonal grains stuck together. A microporosity appeared at the surface of the granules (Fig. 2b). The micropores (1–3  $\mu$ m in width) were noted at the confluence of some polygonal tiles of the pavement (Fig. 2c). SEM also identified shear bands at the surface of some pavement tiles; they have been formed during sintering when lacunae and dislocation occur with the motion of atoms at high temperature. On the granule-fractured surfaces, microporosity was also evidenced between the melted grains.

### Histological Analysis

Remnants of the  $\beta$ -TCP granules were easily identified as composed of numerous elementary grains packed together.

**Fig. 1** X-ray diffractometry (XRD) of the  $\beta$ -TCP granules used in this study

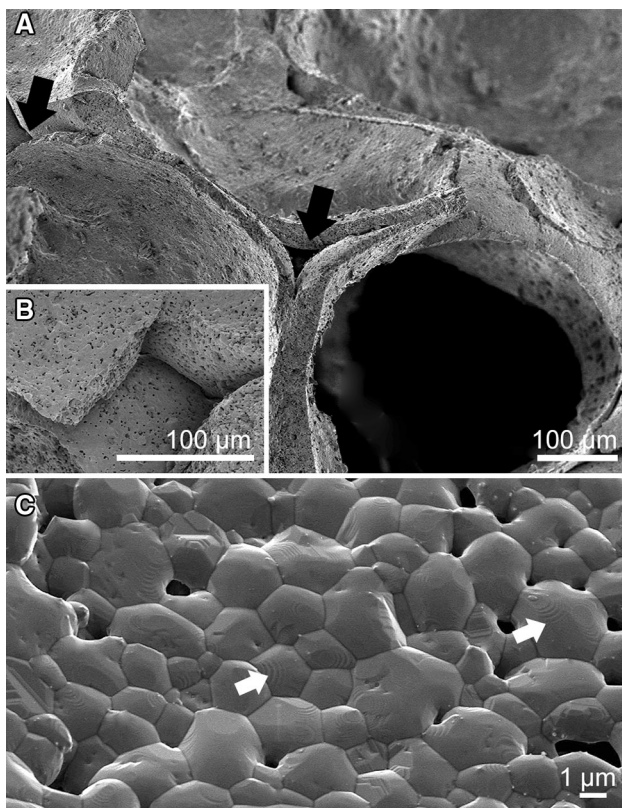
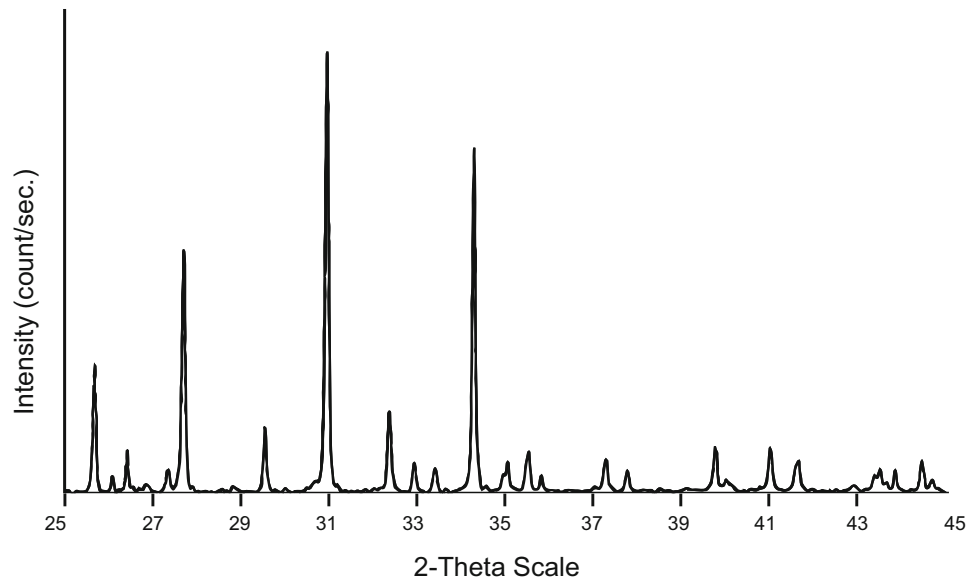


**Fig. 2** **a** Scanning electron microscopy analysis of a  $\beta$ -TCP granule at high magnification showing the concave surfaces (reflecting macroporosity) and the triangular inner porosity due to the removal of the foam during the sintering step (*arrow*). **b** The microporosity between melted grains is shown in an enlarged image. **c** Higher magnification of the surface of a  $\beta$ -TCP granule showing the typical tessellation with the presence of several micropores. Note also the shear bands (*white arrows*) corresponding to dislocation lines created during sintering

Newly formed bone was found directly apposed at the surface of the  $\beta$ -TCP granules and the Goldner trichrome identified different cases: (1) fully mineralized bone directly apposed on the granule; (2) packets of osteoid tissue which have been deposited inside the internal porosity of a granule or as a streak separating  $\beta$ -TCP and mineralized bone; and (3) osteoid seam directly apposed at the surface of the  $\beta$ -TCP granule, corresponding to the beginning of elaboration of a new bone packet by osteoblasts. These different aspects are illustrated in Fig. 3a, b. A mesenchymal reaction composed of fibroblasts, thin collagen fibers, and macrophages was observed in the marrow spaces between bone trabeculae anchored on the granules. Most cells were mononucleated macrophages and plurinucleated osteoclasts remodeling the bone or biomaterial surfaces (Fig. 3c, d). The cytoplasm of the macrophages in the mesenchymal reaction appeared filled with numerous elementary  $\beta$ -TCP grains enlarging the cell. These grains were  $4.6 \pm 0.6 \mu\text{m}$  in width. Under polarized light microscopy, these elementary grains were lightly refringent inside the cytoplasm (Fig. 3e, f). Numerous mast cells clearly identified by the presence of metachromatic cytoplasmic granules were also encountered in the mesenchymal reaction (Fig. 3e, f).

### NanoCT

NanoCT could easily identify  $\beta$ -TCP due to its higher calcium content when compared to the hydroxyapatite of bone. Remnants of the granules were found covered by newly formed bone whose osteocytic lacunae were observed at high magnification. In some areas, the biomaterial appeared surrounded by mineralized bone, indicating a complete osseointegration. The 3D reconstruction



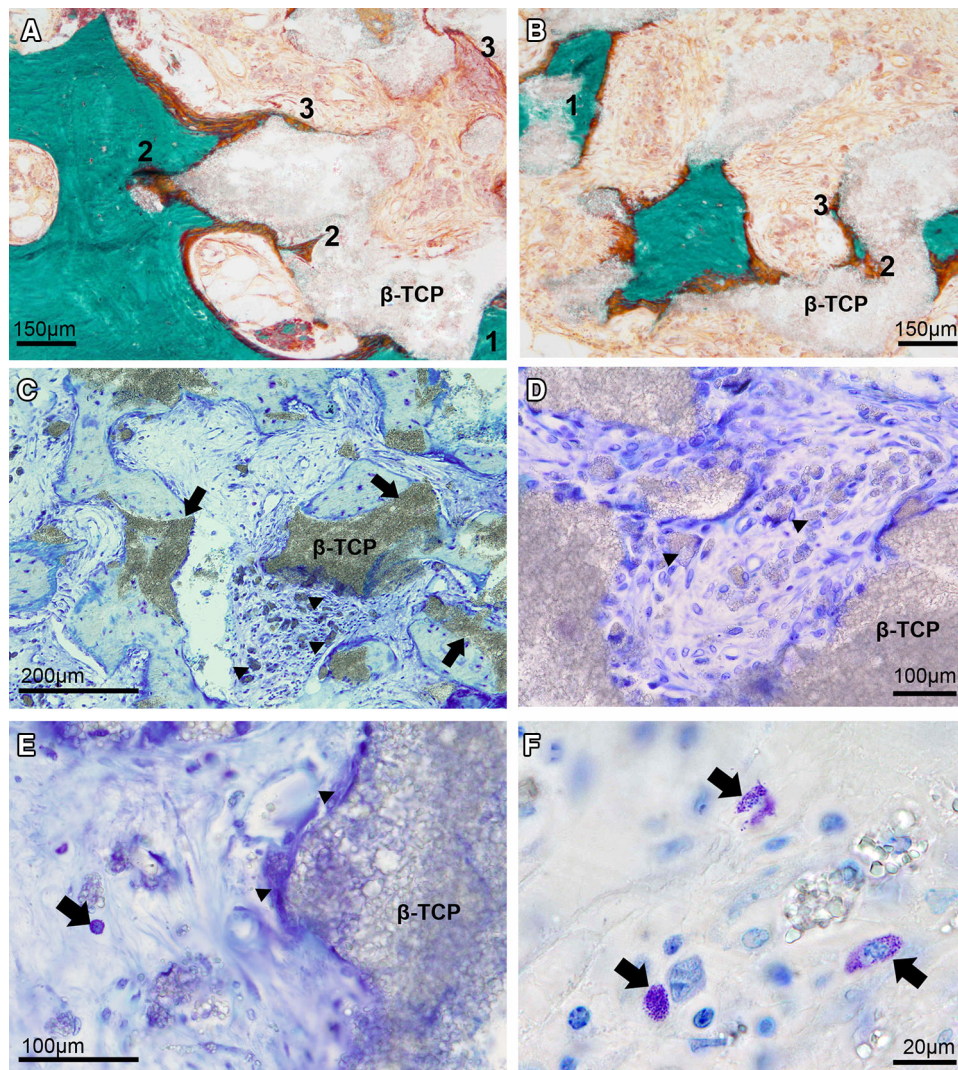


**Fig. 3** Histological analysis on undecalcified bone biopsies. **a** Typical aspect of an osseointegrated  $\beta$ -TCP granule stained with Goldner's trichrome showing mineralized bone in green and osteoid tissue in red;  $\beta$ -TCP is unstained and appears gray. 1—Fully calcified bone in direct contact with the biomaterial; 2—osteoid tissue inside the internal porosity of a granule; 3—osteoid seam in direct contact with the granule and corresponding to the beginning of a new bone structure unit. **b** Same aspect in another patient. **c** Undecalcified section stained with toluidine blue:  $\beta$ -TCP appears in gray, bone trabeculae apposed at the surface of the granules are evidenced (arrows). Note the loose mesenchymal reaction (blue cells) containing numerous macrophages which have

engulfed grains of  $\beta$ -TCP giving them a gray tint (arrowheads). **d** Higher magnification of the mesenchymal reaction containing numerous macrophages filled with  $\beta$ -TCP grains (arrowheads) in another patient. Toluidine blue staining. **e** Erosion of the material by osteoclasts (arrowheads) in direct contact with a granule surface. Macrophages filled with  $\beta$ -TCP grains are in the marrow spaces which contain mast cells (arrow). **f** High magnification of the cells present in the mesenchymal reaction showing both mast cells with numerous metachromatic granules (arrows) and phagocytic cells with refringent  $\beta$ -TCP granules distending the cytoplasm (semi-polarized microscopy) (Color figure online)

models, obtained by volume rendering, appear in Fig. 4. The internal porosity, produced by the polyurethane foam, was evidenced as connected channels with a somewhat triangular section with concave sides. These areas did not fully mineralize and remained radio-lucent. The residual volume of  $\beta$ -TCP in the grafted area varied between 5 and 10%. The most striking aspect was the direct observation of packed elementary grains in the cytoplasm of macrophages present between the trabeculae present in the marrow spaces. Because the cell themselves and the fibers of the

mesenchymal reaction are radio-lucent, these macrophages filled with radiopaque grains seemed floating in the marrow spaces on 3D reconstructions. In some areas, they appeared very numerous giving a 'milky way' appearance (Fig. 4d) which is better appreciated on the video supplementary file.

### Raman Microspectroscopy

Spectrum of the pMMA resin around the samples, determined in areas free of tissue, appears in Fig. 5a where the

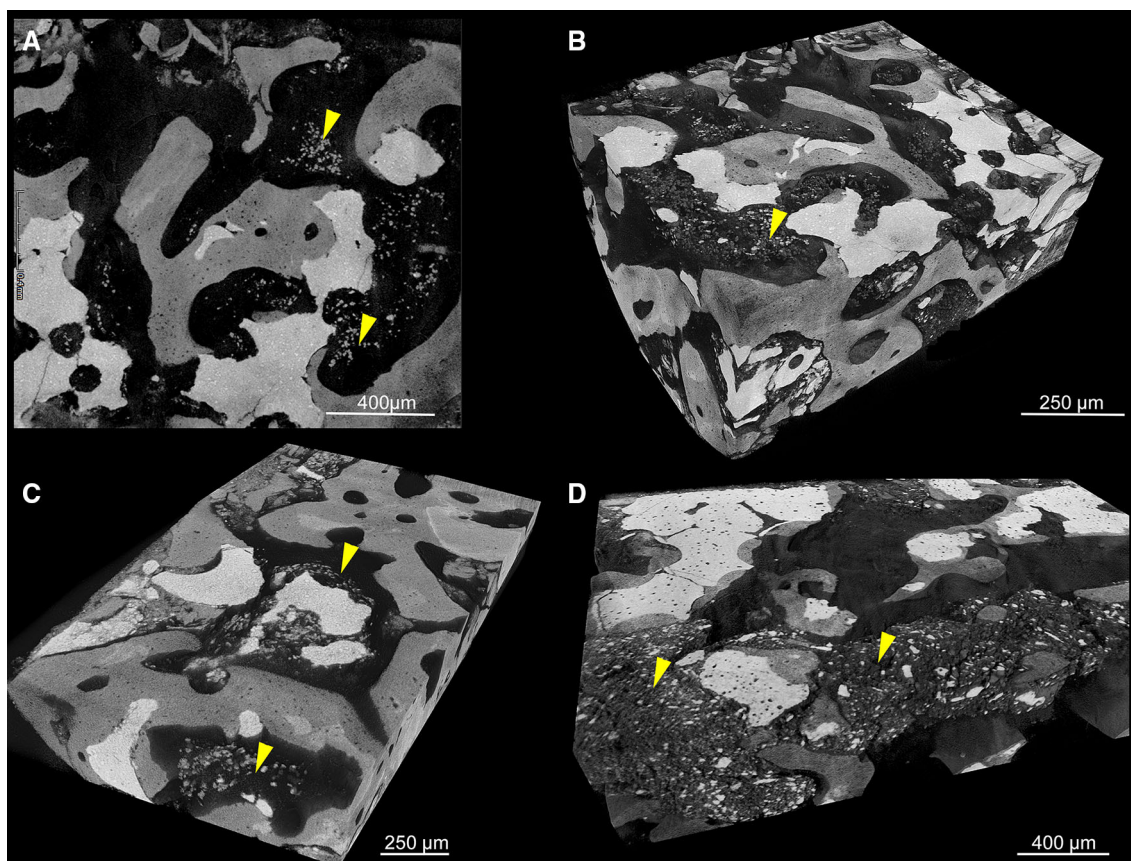


**Fig. 4** Nanocomputed tomography of bone biopsies performed after sinus lift grafting which  $\beta$ -TCP granules. **a** 2D section showing the biomaterial in light gray with fully calcified bone trabeculae (darker gray) apposed directly onto the  $\beta$ -TCP. **b** 3D reconstruction model of the same patient grafted 8 months before the biopsy; **c** Bone biopsy

performed in a patient grafted 9 months before. Note the osseointegration of the granules; **d** Bone biopsy performed 6 months after the graft. In each case, the macrophages containing  $\beta$ -TCP grains (3–5  $\mu$ m in width) are evidenced (yellow arrowhead) and form a “milky way” aspect (Color figure online)

main peaks are labeled. The most typical were at  $611\text{ cm}^{-1}$  ( $-\text{COOCH}_3$ ),  $820\text{ cm}^{-1}$  ( $-\text{CH}_2$ ),  $1735\text{ cm}^{-1}$  ( $-\text{C}=\text{O}$ ), and  $1460\text{ cm}^{-1}$  (CH). The spectrum of pure unembedded  $\beta$ -TCP was determined on isolated granules and is represented in Fig. 4b. The major bands are attributed to the different peaks of phosphate  $959\text{--}970\text{ cm}^{-1}$  for  $\nu_1$ ,  $370\text{--}500\text{ cm}^{-1}$  for the  $\nu_2$ ,  $1030\text{--}1100\text{ cm}^{-1}$  for the  $\nu_3$ , and  $530\text{--}645\text{ cm}^{-1}$  for the  $\nu_4$ . The  $\nu_1$  peak is has a typical bifid appearance. When the granules were embedded in pMMA, the same major peaks were observed together with some specific peaks of pMMA at  $\sim 820$  and  $\sim 1735\text{ cm}^{-1}$ ; however, the  $\nu_1$  peak was modified by the presence of a pMMA band at the same location (Fig. 5c). The other specific peaks of the polymer were masked by those of the phosphate groups. The ratio of the  $820/\nu_1$  phosphate bands was about  $6.7 \pm 2.0\%$  corresponding to the inner micro-porosity between the melted grains composing the granules. The same ratio determined on unembedded grains was  $0.01\%$ . The spectra of the osseointegrated  $\beta$ -TCP granules

in the patients provided similar data to those in the embedded granules; however, the ratio  $820/\nu_1$  phosphate band was significantly increased in this area to  $11.7 \pm 4.6\%$  ( $p = 0.007$ ) versus embedded grains. The spectra were also analyzed in the macrophages of the marrow spaces. A typical spectrum appears in Fig. 4d. The characteristic bands of  $\beta$ -TCP are observed together with the presence of amide I and III bands coming from cell proteins. Two additional peaks at  $750$  and  $1050\text{ cm}^{-1}$  were also observed and corresponded to other cytoplasmic proteins impossible to characterize by this technique. Here again, the presence of the  $\sim 820$  and  $\sim 1735\text{ cm}^{-1}$  bands of the pMMA was evidenced and the ratio of the  $820\text{ cm}^{-1}/\nu_1$  phosphate band was  $33.9 \pm 5.0\%$ , a value significantly increased versus the value obtained in the center of the implanted granule ( $p < 0.001$ ).

The Raman spectrum of the bone matrix of an unembedded human bone is given in Fig. 5. It reveals the classical peaks observed in the bone matrix with a prominent



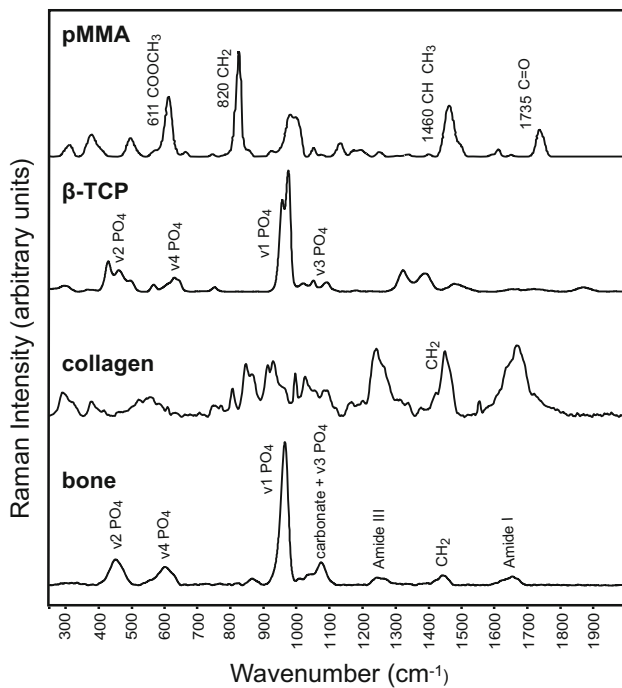


**Fig. 5** Raman microspectroscopic analysis of pMMA used for histological embedding;  $\beta$ -TCP from an unembedded granule; collagen from a demineralized bone specimen; and an unembedded human bone

v<sub>1</sub> phosphate peak at 960–970 cm<sup>-1</sup>, the 1240–1250 cm<sup>-1</sup> peak stands for the amide III, 1660–1678 cm<sup>-1</sup> for the amide I, and 1450 cm<sup>-1</sup> for the -CH<sub>2</sub> group present in all proteins. The Raman spectrum of the bone matrix measured in the grafted patients, at distance from a  $\beta$ -TCP granule, is provided in Fig. 6 and revealed the presence of the typical peaks of bone plus the distinct peaks at ~820 and ~1735 cm<sup>-1</sup> corresponding to the presence of pMMA which has infiltrated the bone matrix. The spectrum determined in an internal pore appears in Fig. 6; this area corresponds to a site filled with osteoid tissue on histological sections; it is similar to area #2 observed in Figs. 3a–b and 4. The amide I and III peaks of the collagen are observed together with the presence of some classical phosphate peaks (v<sub>1</sub> and v<sub>4</sub>) indicating incomplete mineralization. However, the v<sub>2</sub> peak at 400–500 cm<sup>-1</sup> was reduced and an additional peak is noted at ~1350 cm<sup>-1</sup>. The degree of mineralization of the bone matrix was determined in the trabeculae apposed on the granules and in the internal pores which were filled with osteoid tissue on histological sections. It was calculated (i) as the ratio of the v<sub>1</sub> phosphate/amide III band and (ii) as the ratio of the v<sub>2</sub> phosphate/amide III, and was found significantly reduced in the osteoid tissue with both methods: resp 9.3 ± 2.5 versus 15.9 ± 3.9;  $p < 0.0001$  and 0.76 ± 0.74 versus 1.64 ± 0.37;  $p < 0.0001$ . The presence of

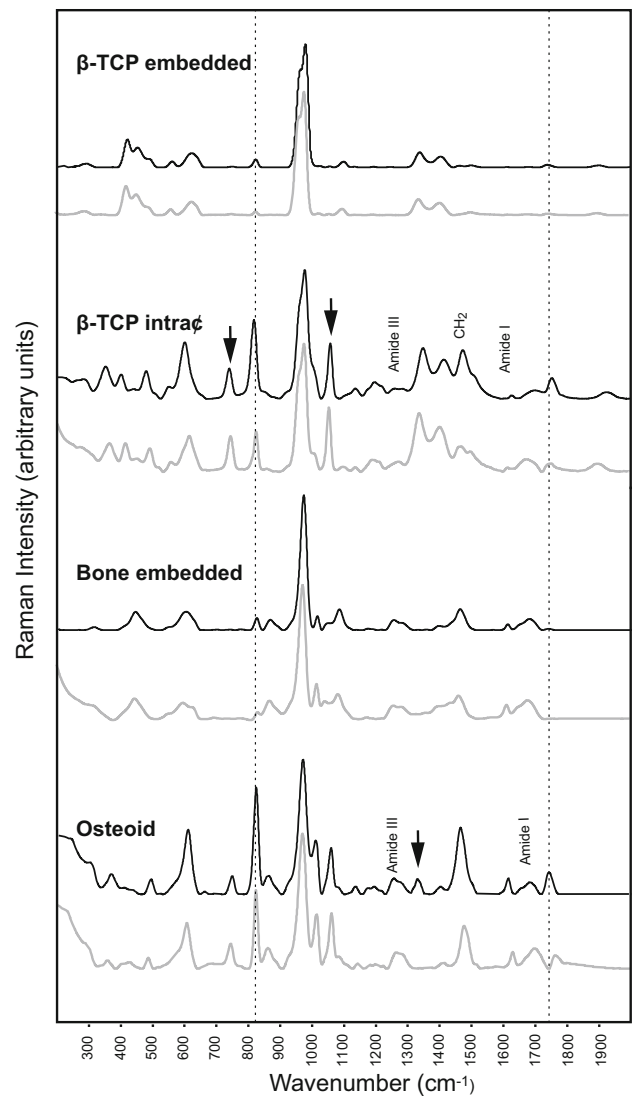


**Fig. 6** Raman microspectroscopic analysis of the different areas analyzed on the bone biopsies in patients grafted with  $\beta$ -TCP; in each case, the original spectrum is provided (*black spectrum*) to show the contribution of pMMA and after subtraction of the pMMA spectrum (*gray spectrum*). The peaks at ~820 and ~1735 cm<sup>-1</sup> indicating the contribution of pMMA are figured as dotted lines.  $\beta$ -TCP granule embedded in pMMA;  $\beta$ -TCP grains in the cytoplasm of macrophages (identified by the characteristic v<sub>4</sub> peak) with the presence of amide I and III of cytoplasmic proteins. Note also the presence of two other peaks at ~700 and 1000 cm<sup>-1</sup> corresponding to other cytoplasmic proteins not observed in bone (*arrows*); bone in the trabeculae at distance from a biomaterial granule; osteoid tissue present inside the internal porosity of a granule

the ~820 and ~1735 cm<sup>-1</sup> bands of the pMMA was evidenced and the ratio of the 820 cm<sup>-1</sup>/v<sub>1</sub> band of the phosphates gave a 39.8 ± 16% in the bone trabeculae and 65.5 ± 9.6% in the areas identified as osteoid tissue ( $p < 0.0001$ ). The ratio obtained in a control bone embedded in pMMA was 14.9 ± 2.7%.

## Discussion

In the present study, undecalcified bone histology together with nanocomputed tomography was used to clarify the fine tissue changes that occur during osseointegration of  $\beta$ -TCP granules in a series of patients after a sinus lift.  $\beta$ -TCP (formula:  $\text{Ca}_3(\text{PO}_4)_2$ ) and hydroxyapatite of the bone matrix (formula:  $\text{Ca}_{10}(\text{PO}_4)_6(\text{OH})_2$ ) can be easily distinguished in nanoCT images due to the higher radio-opacity of the material. The biomaterial is made of 100% of mineral, while the mineral phase only represents 2/3 of the bone matrix [27].

Raman microspectroscopy was used in parallel in specific sites identified by the two methods to evaluate the material and bone during in the grafted area. A similar approach has previously been proposed with complementary histologic, nanoCT, and spectroscopic methods with another biomaterial composed of aragonite [28]. The factors and cellular mechanisms controlling the degradation and osseointegration of orthocalcium phosphate ceramics such as  $\beta$ -TCP are still not completely elucidated. Discrepancies can be noted between *in vitro* studies performed using stimulated cell lines and *in vivo* studies in which the cells take place in integrative physiological programs. This is particularly evident when studying the remodeling of bone and biomaterials which combines the action of bone-resorbing cells (coming from the monocyte/macrophage lineage) with osteoblasts (a highly differentiated form of fibroblast). The histological findings noted in this series of patients confirm our previous observations reported in the same clinical situation [5]. Granules of  $\beta$ -TCP are osseointegrated by a remodeling process combining the activity of plurinucleated giant cells (which express the tartrate-resistant acid phosphatase—data not shown here) and macrophages present in the bone marrow and engulfing  $\beta$ -TCP grains in their cytoplasm. These cells are accompanied by a number of mast cells present in the mesenchymal reaction between the granules and the newly apposed bone. The presence of these cells is poorly understood but they are frequently associated with active osteoblasts in bone-forming areas [29, 30]. Degradation by a double population of phagocyte cells (i.e., osteoclast and macrophages) has been recognized in a large number of Ca/P ceramics [8, 17, 19, 31–33]. Resorption of the biomaterial is associated with a direct apposition of bone at the surface of the granule by active osteoblasts. Numerous authors have confirmed the direct apposition of bone matrix onto the surface of  $\beta$ -TCP granules [5, 8, 34–36]. However, it was found here that osteoid tissue deposited in the deep internal porosity of the granules remained non-mineralized. This was found both on Goldner-stained histologic sections and on the nanoCT analysis which

identified these areas as radio-lucent. Electron microscopic studies have shown that osteoblasts are capable to lay down bone matrix inside the porosity of the material [8]. Here, the inner porosity of the granules, due to the industrial process [21, 37], produced areas that can be filled with osteoid tissue in this closed space, far from the bone/marrow interface. These areas contain collagen and other proteins identified by Raman microspectrometry, together with a small amount of phosphate, (presence of the  $\nu_1$  band, quasi-absence of the  $\nu_2$  peak) and the presence of other proteins not found in the mature and fully mineralized bone matrix ( $\sim 1350 \text{ cm}^{-1}$  peak). It may reflect a reduced access of free  $\text{Ca}^{2+}$  or  $\text{PO}_4^{3-}$  ions in areas far from the bone surfaces or a reduced alkaline phosphatase activity (a key enzyme elaborated by osteoblasts during calcification). This situation resembles of the mineralization defects observed in osteomalacia when streaks of osteoid tissue remain under-mineralized and covered by fully calcified bone. [38, 39].

In this study, nanoCT appeared as a most important tool to evaluate the osseointegration of  $\beta$ -TCP. Previous studies using microcomputed tomography (microCT) on bone biopsies performed in man or animals were found interesting to characterize the bone/biomaterial interface but failed to identify the macrophages in the mesenchymal reaction [5, 6, 40]. NanoCT differs from microCT by the use of polychromatic X-rays allowing to detect more subtle details. In addition, microCT softwares most often use surface rendering algorithms to construct the 3D models. Surface rendering is based on interactive thresholding of the 2D sections for the generation of the 3D models, but it succinctly represents the 3D configuration of complicated objects. The threshold used to make a binary classification decision of voxels on the stack of images produces isovalue contour lines, but either a surface passes through the current voxel or it does not. As a consequence, surface rendering often exhibits false positives (spurious surfaces) or false negatives (abnormal defects on the surfaces), particularly in the presence of small or poorly defined features. Unlike surface rendering, volume rendering used in this study loads the full dataset of the 2D grayscale sections [41]. In this method, no threshold is necessary to compute the geometric representation of the surface and 3D images are formed by directly shading each voxel of the stack and projecting it on the visualization plane. Voxels having transitional values are not misclassified and small or poorly defined features are not lost [42]. Because thresholding is avoided, minute details can be observed at the cell level. Osteocyte lacunae are shown in the newly formed bone together with the presence of the numerous macrophages whose cytoplasm was filled with  $\beta$ -TCP elementary grains. The X-ray absorption property of the material allowed



identification of these cells and their 3D distribution in the mesenchymal reaction corresponds to the histological findings in 2D sections [5, 7, 8]. The evolution of these macrophages filled with  $\beta$ -TCP grains is largely unknown. Whether these cells migrate to the regional lymph nodes (as observed in case of wear debris in orthopedic prostheses) [43] or terminate the degradation of the material locally has not been studied. Dissolution of  $\beta$ -TCP necessitates the action of carbonic anhydrase type II, an enzyme that catalyzes the conversion of  $\text{CO}_2$  and water to carbonic acid which spontaneously produces  $\text{H}^+$  and  $\text{HCO}_3^-$ . The enzyme is normally secreted by osteoclasts to demineralize the bone matrix [44]. Culture experiments have shown that macrophagic cell lines can express carbonic anhydrase II in the presence of CaP biomaterials [17, 45]. However, histochemical identification of the enzyme was not possible in the present study. It is well known that macrophages can adapt their enzyme repertoire to their tissular microenvironment, thus gaining a tissue specialization [46]. In an *in vivo* study in the rabbit, it was found that macrophages having phagocytized numerous  $\beta$ -TCP grains in the grafted area were incapable to phagocyte supplementary fluorescent nano-beads [6]. A limitation of the study could be represented by the use of formalin in the fixative. The Beebe's fixative used in the present study combines the effects of ethanol (suitable for Raman analysis) and formalin (indispensable for cell preservation) [22]. In a systematic assay of different fixatives and embedding media for bone before spectroscopic analysis, it was found that aqueous fixatives such as formalin could cause alteration in the crystallinity of the bone matrix and that alcohol should be preferred [47]. However, alcohol is responsible for a considerable shrinkage of tissues and is no longer recommended for histological analysis [48]. In the present study, the bones biopsies were fixed for a short period of time in a fixative containing predominantly ethanol and a small part of formalin to minimize the shrinking effect of ethanol. The short fixation period minimalizes the effects of formalin as reported by other authors [49–52].

Raman microspectroscopy clearly identified changes in the spectrum of  $\beta$ -TCP depending on the localization of the material. Unembedded  $\beta$ -TCP exhibited a typical bifid  $\nu_1$  peak as reported by others and attributed to a symmetric P–O stretching mode [17, 53–55]. This aspect is lost in  $\beta$ -TCP embedded in pMMA as the 950–1050 peak corresponding to the  $-\text{CH}_3$  group was over imposed [56]. The presence of pMMA was also evidenced by the occurrence of the two other characteristic peaks at  $\sim 820$  and  $\sim 1735$   $\text{cm}^{-1}$ . In the spectrum of the CaP particles internalized in the cytoplasm of the macrophage, the same modified  $\nu_1$  peak was noted together with additional peaks which identified proteins by their amide I and III moieties together with additional peak at  $\sim 750$   $\text{cm}^{-1}$  (probably reflecting the  $-\text{COO}^-$

group of amino acids [57]) and at  $\sim 1000$   $\text{cm}^{-1}$  (reflecting the  $-\text{CC}-$  groups of aromatic amino acids such as Phe) [57, 58]. However, the exact nature of these cytoplasmic proteins cannot be determined by this technique which can only identify specific functional groups [59]. Raman microspectroscopy was also interesting to evaluate the microporosity of  $\beta$ -TCP and the bone hydration as MMA can infiltrate microporosity and substitutes to water in hydrated tissues during histological embedding [23]. The  $\sim 820$   $\text{cm}^{-1}/\nu_1$  phosphate band was significantly increased in the granules of  $\beta$ -TCP implanted in the patients versus  $\beta$ -TCP granule embedded in pMMA. This could reflect the increased diffusion volume reached by a granule after implantation by water from the extracellular fluids. This ratio was considerably increased in the grains phagocytized by the macrophages and present in their cytoplasmic vacuoles. When determined in a control embedded bone block coming from a human cadaver, the  $\sim 820$   $\text{cm}^{-1}/\nu_1$  phosphate ratio was  $14.9 \pm 2.7\%$  corresponding to the volume of diffusion of pMMA in bone determined by histological methods [60]. This ratio was increased in the newly apposed bone onto the  $\beta$ -TCP surfaces and reflected the lowest degree of organization of the bone matrix with a lower mineralization degree. It was significantly increased in the osteoid areas having an increased degree of hydration. In the literature, the most widely band used to determine the degree of mineralization is the  $\sim 960$  phosphate band, characteristic of the carbonated hydroxyapatite [61]. It should be noted that other authors have proposed to use the ratio of the  $\nu_2$  or the  $\nu_4$   $\text{PO}_4/\text{amide III}$  to evaluate the composition of bone mineral because they are independent of the tissue organization [26, 62]. In the present study, the degree of mineralization was computed using the two methods and the results appeared similar and showed a reduction in the osteoid tissue. The contribution of pMMA was also studied by subtracting its spectrum to the original spectrum obtained in the different areas of interest. There was a minor underlying contribution of pMMA and collagen to the  $\nu_1$   $\text{PO}_4$  band and the most contributive bands of collagen are in the  $1000\text{--}1800$   $\text{cm}^{-1}$  region [63]. The  $\sim 820$   $\text{cm}^{-1}$  band of the pMMA corresponds to the  $-\text{CH}_2$  group which is also present as a minor peak in the collagen spectrum. The most characteristic  $-\text{CH}_2$  band of collagen is at  $1450$   $\text{cm}^{-1}$  (similar to the bone matrix).

## Conclusion

Nanocomputed tomography and Raman microspectroscopy are two additional methods to analyze histology of bone grafted with biomaterials. They allow to clearly identify newly degradation processes with the presence of  $\beta$ -TCP

grains in the cytoplasm phagocytic cells. The mechanisms of bone apposition onto the material can also be analyzed with precision. The occurrence of unmineralized osteoid tissue in the internal porosity reflects to the confinement of these areas and was well revealed by the three methods.

**Acknowledgements** The authors thank Mrs Laurence Lechat for secretarial assistance, Mrs N. Retaillieu and S. Lemi re for microCT and histotechnology. E. Paschalis and G. Mabilieu are thanked for helpful discussions. This work was made possible by grants from ANR, program LabCom “NextBone”. The authors thank Kasios, 18 Chemin de la Violette, 31240 L’Union—France—for providing the  $\beta$ -TCP granules.

**Author Contribution** The study was conceived by DC and BG. Surgery and patient handling were done by BG. Experimental analyses were designed by DC and performed by the acknowledged technicians. Histopathological analysis was done by DC. Raman analysis was done by FPG, SEM by BA, and nanoCT by LT and HL. The paper was written by DC and FPG, and the final manuscript was approved by all of the authors.

#### Compliance with Ethical Standards

**Conflict of interest** Florence Pascaretti-Grizon, Bernard Guillaume, Lisa Terranova, Baptiste Arbez, H el ne Libouban, and Daniel Chappard declare that they have no conflict of interest.

**Human and Animal Rights and Informed Consent** An informed consent was obtained from each subject. This experimental protocol was approved by the ethical committee of the French Coll ge d’Implantologie and was done in accordance with the institutional guidelines of the French Ethical Committee and with the 1964 Helsinki declaration and its later amendments.

#### References

1. Böhner M (2010) Resorbable biomaterials as bone graft substitutes. *Mater Today* 13:24–30
2. Guillaume B (2016) Dental implants: a review. *Morphologie* 100:189–198
3. Chappard D, Terranova L, Mallet R, Mercier P (2015) 3D porous architecture of stacks of beta-TCP granules compared with that of trabecular bone: a microCT, vector analysis, and compression study. *Front Endocrinol* 6:161
4. Ndiaye M, Terranova L, Mallet R, Mabilieu G, Chappard D (2015) Three-dimensional arrangement of beta-tricalcium phosphate granules evaluated by microcomputed tomography and fractal analysis. *Acta Biomater* 11:404–411
5. Chappard D, Guillaume B, Mallet R, Pascaretti-Grizon F, Baslé MF, Libouban H (2010) Sinus lift augmentation and beta-TCP: a microCT and histologic analysis on human bone biopsies. *Micron* 41:321–326
6. Nyangoga H, Aguado E, Goyenvalle E, Baslé MF, Chappard D (2010) A non-steroidal anti-inflammatory drug (ketoprofen) does not delay beta-TCP bone graft healing. *Acta Biomater* 6:3310–3317
7. Lu J, Descamps M, Dejou J, Koubi G, Hardouin P, Lemaitre J, Proust JP (2002) The biodegradation mechanism of calcium phosphate biomaterials in bone. *J Biomed Mater Res* 63:408–412
8. Chazono M, Tanaka T, Kitasato S, Kikuchi T, Marumo K (2008) Electron microscopic study on bone formation and bioresorption after implantation of beta-tricalcium phosphate in rabbit models. *J Orthop Sci* 13:550–555
9. Takayanagi H (2007) Osteoimmunology: shared mechanisms and crosstalk between the immune and bone systems. *Nat Rev Immunol* 7:292–304
10. Palmer JA, Abberton KM, Mitchell GM, Morrison WA (2014) Macrophage phenotype in response to implanted synthetic scaffolds: an immunohistochemical study in the rat. *Cells Tissues Organs* 199:169–183
11. Kajahn J, Franz S, Rueckert E, Forstreuter I, Hintze V, Moeller S, Simon JC (2012) Artificial extracellular matrices composed of collagen i and high sulfated hyaluronan modulate monocyte to macrophage differentiation under conditions of sterile inflammation. *Biomater* 2:226–273
12. Londono R, Badylak SF (2015) Biologic scaffolds for regenerative medicine: mechanisms of in vivo remodeling. *Ann Biomed Eng* 43:577–592
13. Chen Z, Wu C, Gu W, Klein T, Crawford R, Xiao Y (2014) Osteogenic differentiation of bone marrow mscs by  $\beta$ -tricalcium phosphate stimulating macrophages via bmp2 signalling pathway. *Biomaterials* 35:1507–1518
14. Beuvelot J, Pascaretti-Grizon F, Filmon R, Moreau MF, Baslé MF, Chappard D (2011) In vitro assessment of osteoblast and macrophage mobility in presence of  $\beta$ -TCP particles by videomicroscopy. *J Biomed Mater Res Part A* 96:108–115
15. Li SP, Dai HL, Yan YH, Cao XY, Zheng QX (2005) Effect of macrophage on degradation of  $\beta$ -TCP ceramics. *Key engineering materials*. Trans Tech Publications, Zurich, pp 549–552
16. Xia Z, Zhu T, Du J, Zheng Q, Wang L, Li S, Chang C, Fang S (1994) Macrophages in degradation of collagen/hydroxylapatite (CHA), beta-tricalcium phosphate ceramics (TCP) artificial bone graft. An in vivo study. *Chin Med J (Engl)* 107:845–849
17. Detsch R, Schaefer S, Deisinger U, Ziegler G, Seitz H, Leukers B (2010) In vitro-osteoclastic activity studies on surfaces of 3D printed calcium phosphate scaffolds. *J Biomater Appl* 26:359–380
18. Choy J, Albers CE, Siebenrock KA, Dolder S, Hofstetter W, Klenke FM (2014) Incorporation of rankl promotes osteoclast formation and osteoclast activity on beta-TCP ceramics. *Bone* 69:80–88
19. Kucera T, Spöner P, Urban K, Kohout A (2014) Histological assessment of tissue from large human bone defects repaired with beta-tricalcium phosphate. *Eur J Orthop Surg Traumatol* 24:1357–1365
20. Schwartzwalder K, Somers H, Somers AV (1963) Method of making porous ceramics. In: 3090094 A, US Patent
21. Filmon R, Retaillieu-Gaborit N, Brossard G, Grizon-Pascaretti F, Baslé MF, Chappard D (2009) Preparation of  $\beta$ -TCP granular material by polyurethane foam technology. *Image Anal Stereol* 28:1–10
22. Beebe K (2000) Alcohol/xylene: the unlikely fixative/dehydrant/clearant. *J Histotechnol* 23:45–50
23. Paschalis EP, Fratzl P, Gamsjaeger S, Hassler N, Brozek W, Eriksen EF, Rauch F, Glorieux FH, Shane E, Dempster D, Cohen A, Recker R, Klaushofer K (2015) Aging versus postmenopausal osteoporosis: bone composition and maturation kinetics at actively-forming trabecular surfaces of female subjects aged 1–84 years. *J Bone Miner Res* 31:347–357
24. Chappard D (2014) Technical aspects: How do we best prepare bone samples for proper histological analysis? In: Heymann D (ed) *Bone cancer: progression and therapeutic approaches*. Academic Press, Elsevier, London, pp 111–120
25. Akkus O, Polyakova-Akkus A, Adar F, Schaffler MB (2003) Aging of microstructural compartments in human compact bone. *J Bone Miner Res* 18:1012–1019

26. Kazanci M, Fratzl P, Klaushofer K, Paschalis EP (2006) Complementary information on in vitro conversion of amorphous (precursor) calcium phosphate to hydroxyapatite from Raman microspectroscopy and wide-angle X-ray scattering. *Calcif Tissue Int* 79:354–359
27. Robey PG, Boskey AL (2009) The composition of bone. In: ASBMR (ed) *Primer on the bone metabolic diseases and disorders of mineral metabolism*, 7th edn. Wiley, Hoboken, pp 32–38
28. Pascaretti-Grizon F, Libouban H, Camprasse G, Camprasse S, Mallet R, Chappard D (2014) The interface between naere and bone after implantation in the sheep: a nanotomographic and raman study. *J Raman Spectrosc* 45:558–564
29. Chiappetta N, Gruber B (2006) The role of mast cells in osteoporosis. *Semin Arthritis Rheum* 36:32–36
30. Saffar JL, Klapisz-Wolikow M (1990) Changes in mast cell number during the activation phase of an induced synchronized remodeling sequence in the rat. *Bone* 11:369–372
31. Baslé MF, Chappard D, Grizon F, Filmon R, Delecric J, Daculsi G, Rebel A (1993) Osteoclastic resorption of ca-p biomaterials implanted in rabbit bone. *Calcif Tissue Int* 53:348–356
32. Zerbo IR, Zijderveld SA, de Boer A, Bronckers AL, de Lange G, ten Bruggenkate CM, Burger EH (2004) Histomorphometry of human sinus floor augmentation using a porous beta-tricalcium phosphate: a prospective study. *Clin Oral Implant Res* 15:724–732
33. Monchau F, Lefevre A, Descamps M, Belquin-Myrdycz A, Laffargue P, Hildebrand H (2002) In vitro studies of human and rat osteoclast activity on hydroxyapatite,  $\beta$ -tricalcium phosphate, calcium carbonate. *Biomol Engin* 19:143–152
34. Kotani S, Fujita Y, Kitsugi T, Nakamura T, Yamamuro T, Ohtsuki C, Kokubo T (1991) Bone bonding mechanism of beta-tricalcium phosphate. *J Biomed Mater Res* 25:1303–1315
35. Chiba S, Anada T, Suzuki K, Saito K, Shiwaku Y, Miyatake N, Baba K, Imaizumi H, Hosaka M, Itoi E (2016) Effect of resorption rate and osteoconductivity of biodegradable calcium phosphate materials on the acquisition of natural bone strength in the repaired bone. *J Biomed Mater Res Part A* 104:2833–2842
36. Gaasbeek RD, Toonen HG, van Heerwaarden RJ, Buma P (2005) Mechanism of bone incorporation of  $\beta$ -TCP bone substitute in open wedge tibial osteotomy in patients. *Biomaterials* 26:6713–6719
37. Terranova L, Libouban H, Mallet R, Chappard D (2015) Analysis of beta-tricalcium phosphate granules prepared with different formulations by nano-computed tomography and scanning electron microscopy. *J Artif Organs* 18:338–345
38. Aaron JE, Gallagher JC, Nordin BE (1974) Seasonal variation of histological osteomalacia in femoral-neck fractures. *Lancet* 2:84–85
39. Meunier PJ (1980) Bone biopsy in diagnosis of metabolic bone disease. In: Cohn DV, Talmage RV, Matthews JL (eds) *Hormonal control of bone metabolism*. Proceedings of the 7th international conference calcium regulating hormones. Excerpta Medica, pp. 109–107
40. Aguado E, Pascaretti-Grizon F, Gaudin-Audrain C, Goyenvallée E, Chappard D (2014) Beta-TCP granules mixed with reticulated hyaluronic acid induce an increase in bone apposition. *Biomed Mater* 9:015001
41. Kuszyk BS, Heath DG, Bliss DF, Fishman EK (1996) Skeletal 3-d ct: advantages of volume rendering over surface rendering. *Skeletal Radiol* 25:207–214
42. Drebin RA, Carpenter L, Hanrahan P (1988) Volume rendering. *ACM Siggraph Computer Graphics*. ACM, New York, pp 65–74
43. Baslé MF, Bertrand G, Guyetant S, Chappard D, Lesourd M (1996) Migration of metal and polyethylene particles from articular prostheses may generate lymphadenopathy with histiocytosis. *J Biomed Mater Res* 30:157–163
44. Riihonen R, Supuran CT, Parkkila S, Pastorekova S, Väänänen HK, Laitala-Leinonen T (2007) Membrane-bound carbonic anhydrases in osteoclasts. *Bone* 40:1021–1031
45. Schaefer S, Detsch R, Uhl F, Deisinger U, Ziegler G (2011) How degradation of calcium phosphate bone substitute materials is influenced by phase composition and porosity. *Adv Eng Mater* 13:342–350
46. Stout RD, Jiang C, Matta B, Tietzel I, Watkins SK, Suttles J (2005) Macrophages sequentially change their functional phenotype in response to changes in microenvironmental influences. *J Immunol* 175:342–349
47. Aparicio S, Doty S, Camacho N, Paschalis E, Spevak L, Mendelsohn R, Boskey A (2002) Optimal methods for processing mineralized tissues for Fourier transform infrared microspectroscopy. *Calcif Tissue Int* 70:422–429
48. Carson FL, Hladik C (2009) Fixation. In: Carson FL, Hladik C (eds) *Histotechnology: A Self-Instructional Text*. American Society for Clinical Pathology Press, Chicago, IL, pp 9–13
49. Strawn S, White J, Marshall G, Gee L, Goodis H, Marshall S (1996) Spectroscopic changes in human dentine exposed to various storage solutions—short term. *J Dent* 24:417–423
50. Mason JT, O’leary TJ (1991) Effects of formaldehyde fixation on protein secondary structure: a calorimetric and infrared spectroscopic investigation. *J Histochem Cytochem* 39:225–229
51. Pleshko NL, Boskey AL, Mendelsohn R (1992) An infrared study of the interaction of polymethyl methacrylate with the protein and mineral components of bone. *J Histochem Cytochem* 40:1413–1417
52. Pleshko NL, Boskey AL, Mendelsohn R (1992) An FT-IR microscopic investigation of the effects of tissue preservation on bone. *Calcif Tissue Int* 51:72–77
53. De Aza P, Santos C, Pazo A, De Aza S, Cusco R, Artus L (1997) Vibrational properties of calcium phosphate compounds. 1. Raman spectrum of  $\beta$ -tricalcium phosphate. *Chem Mater* 9:912–915
54. Kumar PN, Mishra SK, Kannan S (2015) Probing the limit of magnesium uptake by  $\beta$ -tricalcium phosphate in biphasic mixtures formed from calcium deficient apatites. *J Solid State Chem* 231:13–19
55. Quillard S, Paris M, Deniard P, Gildenhaar R, Berger G, Obadia L, Bouler J-M (2011) Structural and spectroscopic characterization of a series of potassium-and/or sodium-substituted  $\beta$ -tricalcium phosphate. *Acta Biomater* 7:1844–1852
56. Willis H, Zichy V, Hendra P (1969) The laser-Raman and infrared spectra of poly (methyl methacrylate). *Polymer* 10:737–746
57. Nabiev IR, Savchenko VA, Efremov ES (1983) Surface-enhanced Raman spectra of aromatic amino acids and proteins adsorbed by silver hydrosols. *J Raman Spectrosc* 14:375–379
58. Frushour BG, Koenig JL (1975) Raman scattering of collagen, gelatin, and elastin. *Biopolymers* 14:379–391
59. Movasaghi Z, Rehman S, Rehman IU (2007) Raman spectroscopy of biological tissues. *Appl Spectrosc Rev* 42:493–541
60. Boer H, van Eek WH (1979) The penetration of the embedding medium methyl methacrylate in undecalcified bone. *Microsc Acta* 81:181–188
61. Mandair GS, Morris MD (2015) Contributions of Raman spectroscopy to the understanding of bone strength. *Bonekey Rep* 4:620
62. Gamsjaeger S, Masic A, Roschger P, Kazanci M, Dunlop JW, Klaushofer K, Paschalis EP, Fratzl P (2010) Cortical bone composition and orientation as a function of animal and tissue age in mice by Raman spectroscopy. *Bone* 47:392–399
63. Gullekson C, Lucas L, Hewitt K, Kreplak L (2011) Surface-sensitive Raman spectroscopy of collagen I fibrils. *Biophys J* 100:1837–1845